On the Role of Heterojunctions of Core-shell Heterostructures in Gas Sensing

Muhammad Hamid Raza[1], Roberto Di Chio[2], Kaveh Movlaee[2], Patrick Amsalem[3], Norbert Koch[3,4], Nicolae Barsan[5], Giovanni Neri[2], Nicola Pinna[1]*

1 -Institut für Chemie and IRIS Adlershof, Humboldt-Universität zu Berlin, Brook-Taylor-Str. 2, 12489 Berlin, Germany

2 -Department of Engineering, University of Messina, C.Da Di Dio, I-98166 Messina, Italy

3 -Institut für Physik and IRIS Adlershof, Humboldt-Universität zu Berlin, Brook-Taylor-Str. 2, 12489 Berlin, Germany

4 -Helmholtz-Zentrum Berlin GmbH, Albert-Einstein-Str. 15, 12489 Berlin, Germany

5 - Institute of Physical and Theoretical Chemistry, University of Tübingen, Auf der Morgenstelle 15, 72076 Tübingen, Germany

* Corresponding Author E-mail: nicola.pinna@hu-berlin.de

The as-synthesized CNT-NiO(x), CNT-SnO$_2$(y), CNT-NiO(x)-SnO$_2$(y) and CNT-SnO$_2$(y)-NiO(x) CSHS samples were thoroughly characterized for their structures, microstructures and morphologies, and chemical states using powder X-ray diffraction (pXRD), transmission electron microscopy (TEM) and X-ray photoelectron spectroscopy (XPS). The authors recommend the cited references for further details on any of the procedures.[1-6]

Powder X-ray Diffraction

The structure and phase composition of the as-synthesized samples were analysed by powder X-ray diffraction (pXRD). **Figure S1** shows pXRD patterns for pristine-CNTs and NiO and SnO$_2$-coated CNTs samples, namely CNT-NiO(200), CNT-SnO$_2$(50), CNT-SnO$_2$(50)-NiO(200) and CNT-NiO(200)-SnO$_2$(50) core-shell heterostructures (CSHS). The diffractions centred at 11.9° (2θ) can be attributed to the (002) plane for the hexagonal graphitic carbon structure (space group: P63mc (186), ICDD: 00-073-1523) from CNTs substrate. The diffractions located at 16.9°, 19.54°, and 27.8° correspond to (111), (200), and (220) planes of the rock salt phase of NiO, respectively (space group: Fm$\overline{3}$m (225), ICDD: 00-073-1523). The broad diffraction peaks show the nanocrystalline nature of the NiO deposited film.[7] This is in-line to our already reported results for the ALD-NiO on different substrates. As expected for this very thin film of NiO with 200 ALD cycles (ca. 5.7 6.5 nm), the diffractions intensity is quite low. However, our earlier studies with higher ALD cycles, *i.e.* with further increasing the thickness of the NiO film, showed that these reflection related to the rock-salt NiO phase became more pronounced.[8] The samples coated with SnO$_2$ only, or NiO and SnO$_2$ in any sequence (*i.e.,* CNT-NiO(x)-SnO$_2$(y) and CNT-SnO$_2$(y)-NiO(x)), show distinctive diffractions related to the cassiterite phase of SnO$_2$. The diffractions peaks located at (2θ) 15.56°, 17.36°, 17.89°, 19.35°, 23.38° and 27.54° correspond to (101), (200), (111), (210), (211) and (310) planes of the tetragonal phase of SnO$_2$, respectively (space group: P42/mnm (136), ICDD: 00-003-0439). The diffraction at 12.26° corresponds to (110) plane of SnO$_2$ (cassiterite phase) is overlapped with the (002) diffraction from the back ground of the CNT substrate. There is no diffraction which can be seen for the any other phase confirming the purity of the cassiterite SnO$_2$ and cubic NiO phases in the respective samples.
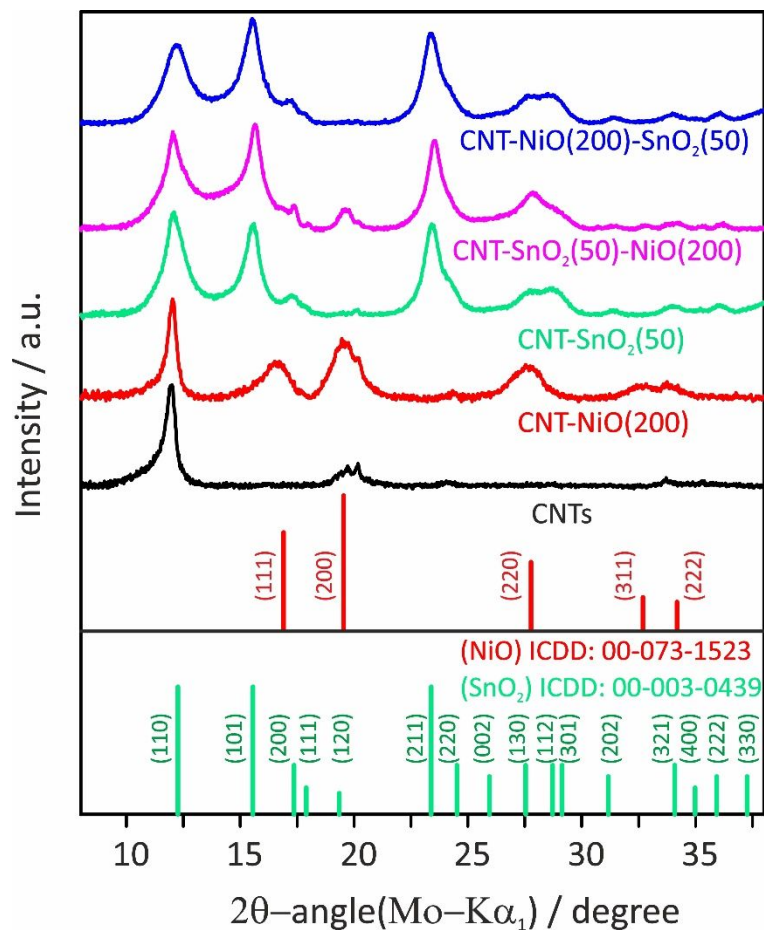
Figure S1. pXRD patterns of CNT-NiO(200), CNT-SnO$_2$(50), CNT-SnO$_2$(50)-NiO(200) and CNT-NiO(200)-SnO$_2$(50) CSHS samples. The pXRD pattern recorded for pristine CNTs is shown (black) as a reference of the substrate background.

Transmission Electron Microscopy

Table S1. Detail of the CNT-$_{n,p}$MOS and CNT-$_{n,p}$MOS-$_{p,n}$MOS core-shell heterostructures along with the average shell thicknesses calculated from TEM micrographs and spectroscopic ellipsometry.

| Sample number	Samples	Transmission electron microscopy (TEM)		Spectroscopic ellipsometry (SE)	
		Thickness NiO (nm)	**Thickness SnO$_2$ (nm)**	**Thickness NiO (nm)**	**Thickness SnO$_2$ (nm)**
I	CNT-SnO$_2$(20)	---	2.9	---	3.3
II	CNT-SnO$_2$(50)	---	8.5	---	9.3
III	CNT-SnO$_2$(100)	---	17	---	18.1
IV	CNT-NiO(200)	6.3	---	6.7	---
V	CNT-SnO$_2$(25)-NiO(200)	5.5	3.5	6.4	3.7
VI	CNT-SnO$_2$(50)-NiO(200)	5.7	8.4	6.5	9.0
VII	CNT-SnO$_2$(50)-NiO(350)	9.5	7.7	9.8	8.8
VIII	CNT- NiO(200)-SnO$_2$(50)	5.9	7.3	8.5	8.8
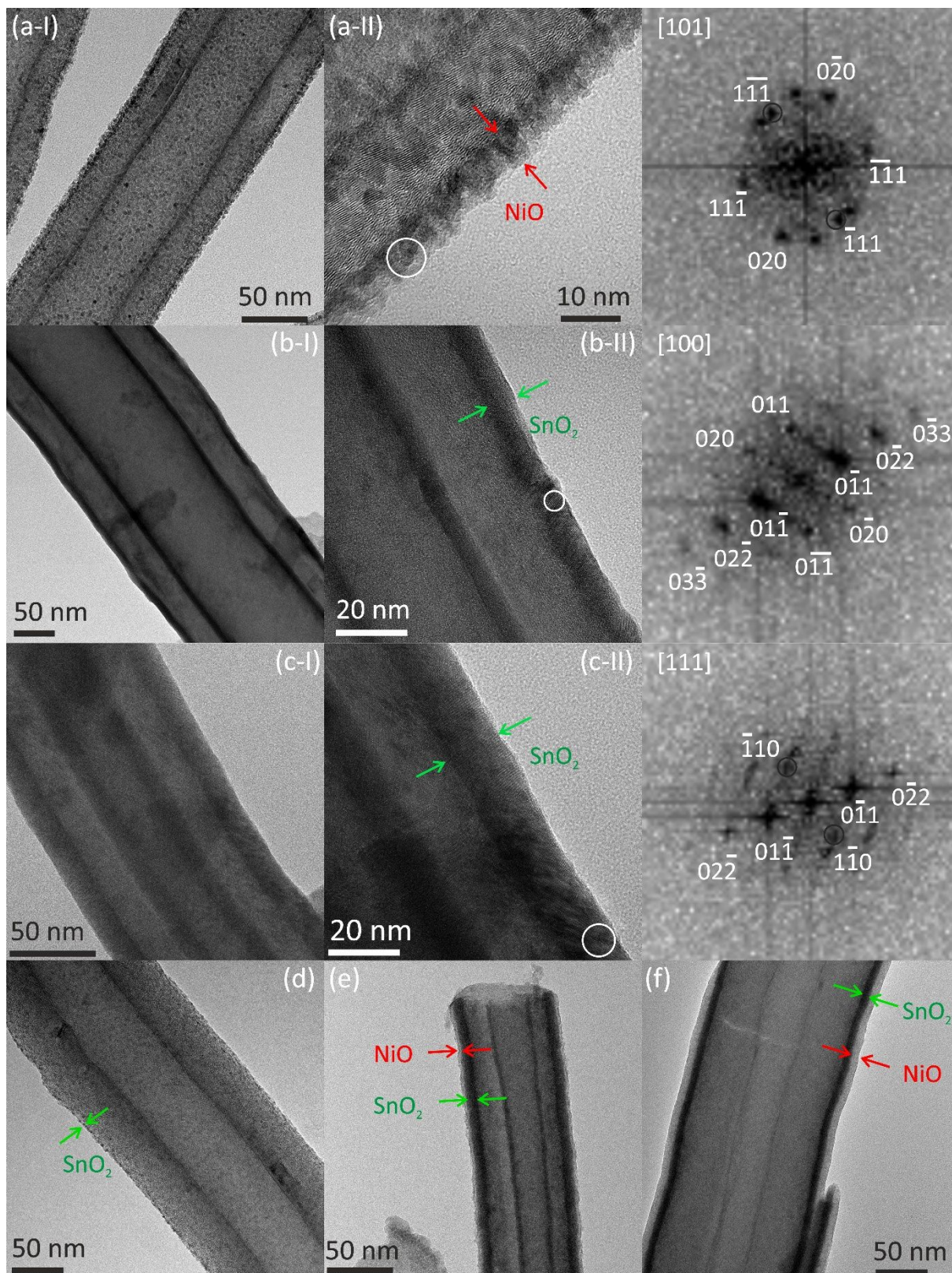
Figure S2. BF-TEM and HRTEM micrographs, and the corresponding power-spectrum for (a) CNT-NiO(200), (b) CNT-SnO$_2$(50) and (c) CNT-SnO$_2$(100) CSHS. BF-TEM micrographs for (d) CNT-SnO$_2$(20), (e) CNT-SnO$_2$(50)-NiO(200) and (f) CNT-SnO$_2$(50)-NiO(350) CSHS. The power spectra shown correspond to the encircled region in the same panel-row.
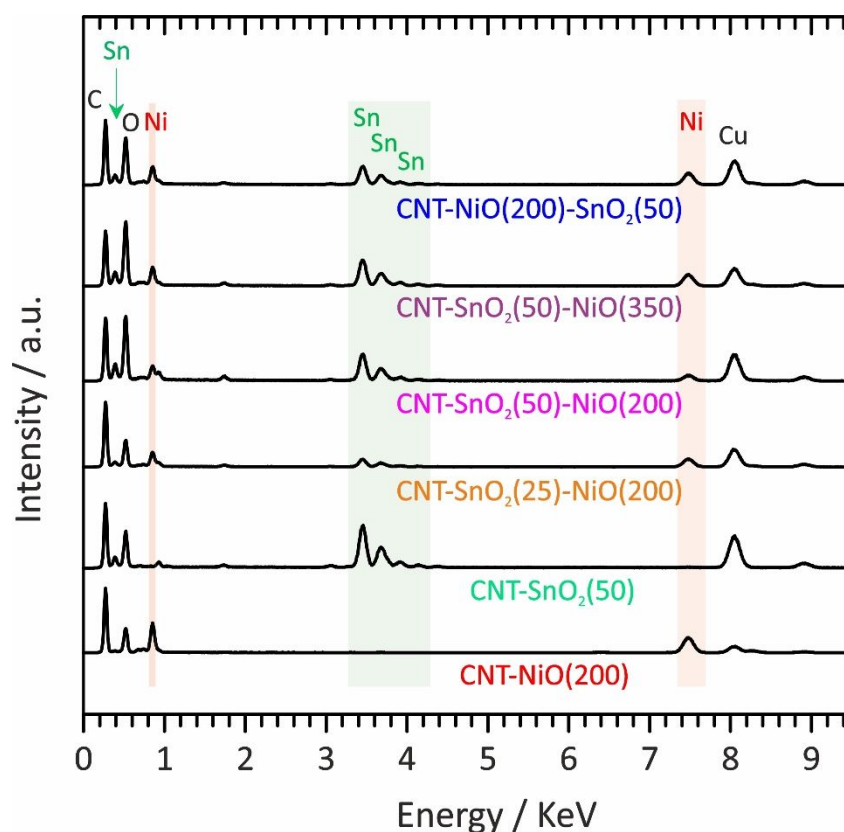
Figure S3. EDX spectra for CNT-NiO(200), CNT-SnO$_2$(50), CNT-SnO$_2$(25)-NiO(200), CNT-SnO$_2$(50)-NiO(200), CNT-SnO$_2$(50)-NiO(350) and CNT-NiO(200)-SnO$_2$(50) CSHS analyzed on a copper TEM-grid.

X-ray and Ultraviolet Photoelectron Spectroscopy

Figure S4 shows the XPS survey spectra of all of the bare-CNTs, CNT-NiO(200), CNT-SnO$_2$(50), CNT-SnO$_2$(50)-NiO(200) and CNT-NiO(200)-SnO$_2$(50) CSHS samples. All of the NiO-terminated heterostructures show Ni-signals marked as Ni 2p and Ni LMM. Similarly, all of the SnO$_2$-terminated heterostructures show typical Sn 4d, Sn 3d and Sn MNN signals marked accordingly (**Figure S4**). The intensity of the Sn signals became lower in CNT-SnO$_2$(50)-NiO(200) as compared to the CNT-SnO$_2$(50) and CNT-NiO(200)-SnO$_2$(50) CSHS, confirming a comformal and homogeneous coverage of the top surface with NiO film (thickness approx. 5.8-6.3 nm, *cf*. HRTEM) in these heterostructures. On the other hand, NiO-related signals cannot be detected in and CNT-NiO(200)-SnO$_2$(50) sample, confirming a homogeneous coverage of the top surface with a SnO$_2$ film (thickness approx. 8-9 nm, *cf*. HRTEM).
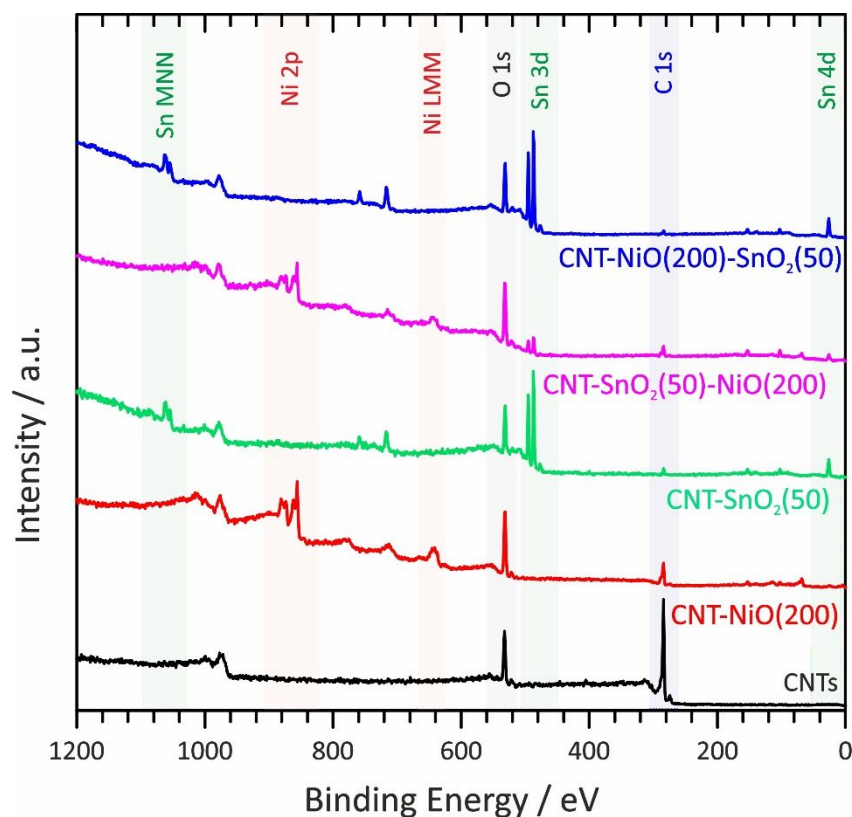
Figure S4. XPS survey spectra of bare-CNTs, CNT-NiO(200), CNT-SnO$_2$(50), CNT-SnO$_2$(50)-NiO(200) and CNT-NiO(200)-SnO$_2$(50) CSHS.

The chemical states of the SnO$_2$ and NiO films deposited onto the CNTs were analysed by looking at X-ray-induced core level and Auger electrons spectroscopy, **Figure S5 8**. **Figure S5a** shows the Sn 3d$_{5/2}$ X-ray photoelectron spectrum of SnO$_2$-coated CNTs (CNT-SnO$_2$(50)). The Sn 3d$_{5/2}$ peak maximum is found at 486.95 eV binding energy (BE). However, it is notoriously difficult to rely only on the Sn 3d core levels BE to derive the oxidation state of Sn.[9-11] Therefore, we additionally examined the corresponding X-ray induced Sn MNN Auger spectra with the M$_5$N$_{45}$N$_{45}$ peak is located at 431.9 eV Kinetic energy (KE), **Figure S5b**. A close inspection of the Sn MNN spectrum reveals strong similarity to that of SnO$_2$ in terms of line-shape and energy position, and substantial differences as compared to those of SnO.[9,11] Therefore, we infer that the ALD growth results in the formation of SnO$_2$, which is further substantiated below by looking at the Auger parameter and the related Wagner plot (**Figure S8b**).

Figure S5c,d shows the X-ray induced Ni 2p core level and Ni LMM Auger spectra of NiO-coated CNTs (CNT-NiO(200)). For the Ni 2p$_{3/2}$, the broad feature centred at 861.2 eV is mainly due to the complex multiplet splitting and to the number of possible final states due to the strong overlap of the Ni and O orbitals.[12] Most relevant is the peak at 856.5 eV BE, which is due to the formation of hydroxide-terminated NiO, Ni(OH)$_2$, in the surface region.[2,6,13-14] We also remark that no characteristic peak of NiO, usually found around 854 ($\pm$ 0.5) eV BE, can be observed. This suggests that hydroxylation of the surface occurs rapidly, at least within the time frame of sample transfer from the ALD chamber to the photoemission setup.[2,14]

To confirm the formation of NiO in the bulk, we additionally proceeded with mild Ar-ion sputtering (500 eV; Δt = 60 s; sample current I_s = 1 μA) of the sample. Importantly, the results of the sputtered sample, which are shown in **Figure S6**, reveal the emergence of a low energy component at 853.5 eV BE in the Ni $2p_{3/2}$ spectrum (**Figure S6a**), which can readily be attributed to the presence NiO.[6,8,13-14] Further confirmation of the surface and bulk nickel oxide compounds (as already confirmed also by XRD, SAED, *cf.* **Figure 1 and S1,2**) is provided by looking at the Auger LMM spectra displayed in **Figure S6b**, which shows an energy shift of 1.3 eV of the $L_3M_{45}M_{45}$ peak to higher KE after sputtering, in very good agreement with existing reports of the Auger spectra of Ni(OH)$_2$ and NiO (**Figure S8a**).[13]

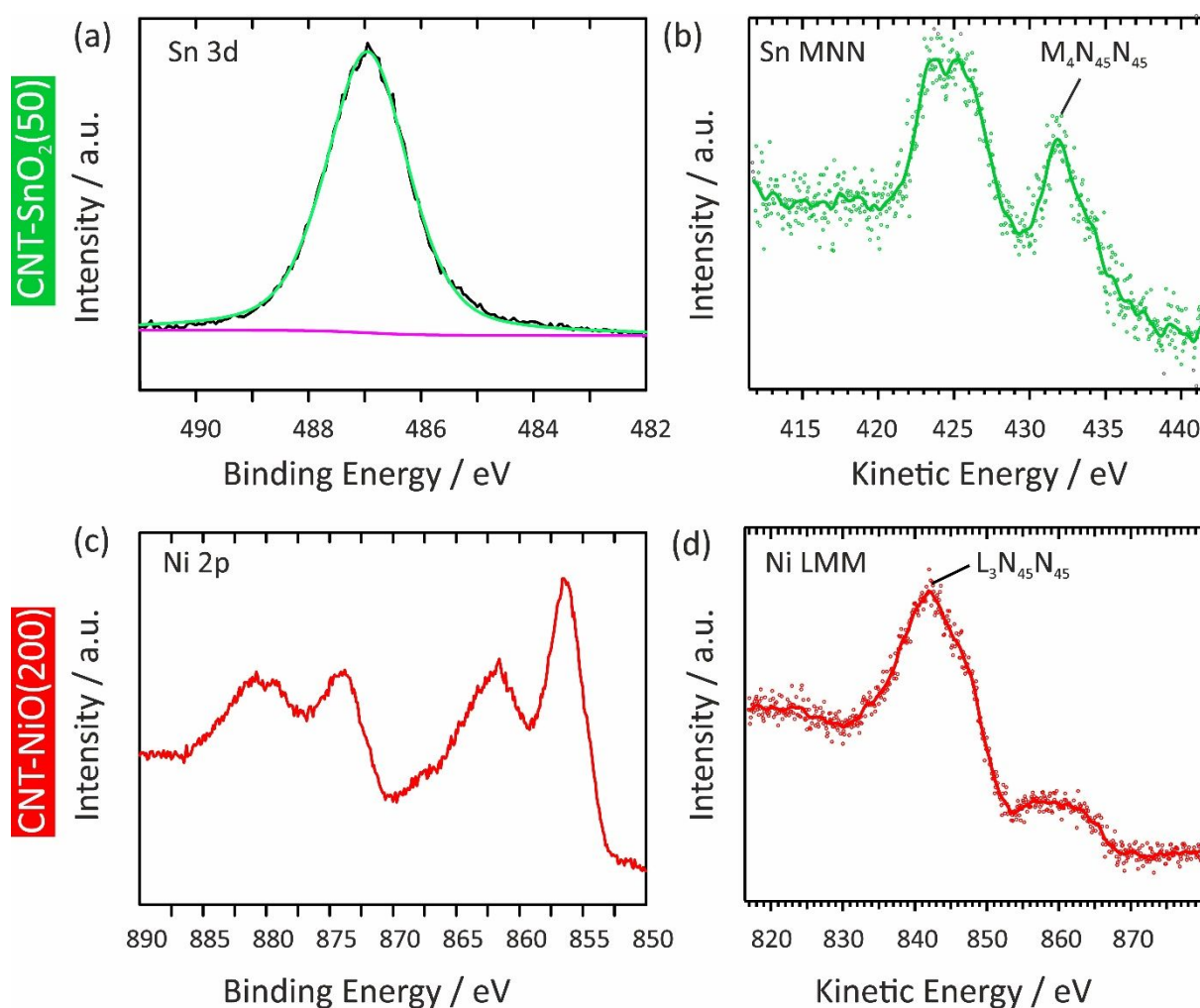**Figure S5**. (a) Sn 3d photoelectron spectrum and (b) Sn MNN Auger spectrum of SnO$_2$-coated CNTs (CNT-SnO$_2$(50) CSHS). (c) Ni 2p2/3 photoelectron spectrum and (d) Ni LMM Auger spectrum of NiO-coated CNTs (CNT-NiO(200) CSHS).
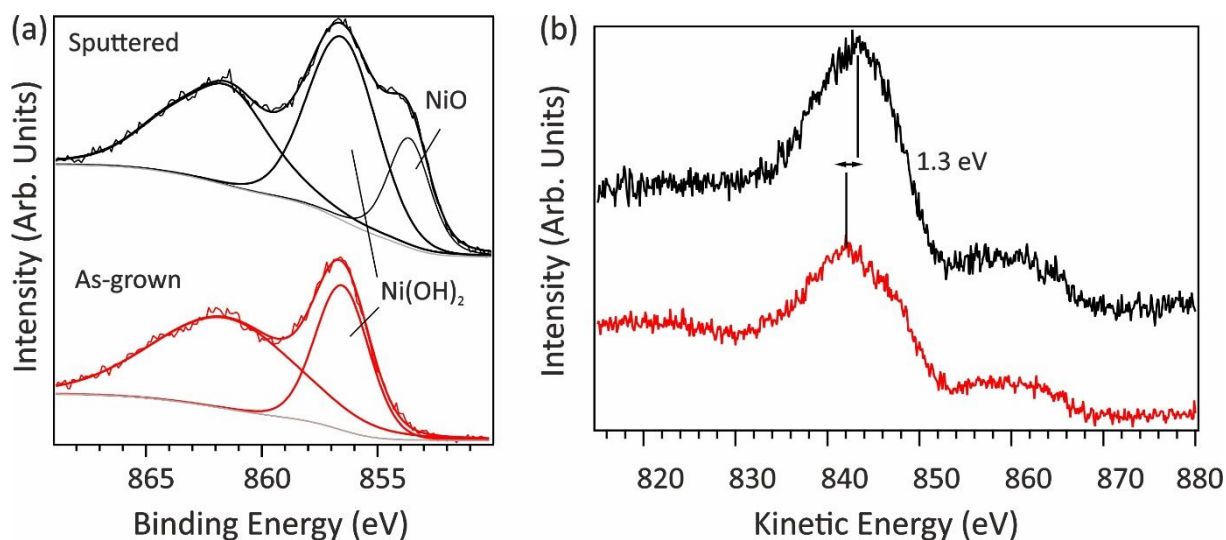
Figure S6. (a) Ni 2p3/2 and (b) Ni LMM spectra of as-grown (red) and mildly Ar-ion sputtered (black) CNT-NiO(200) CSHS revealing the presence of NiO after sputtering.

Figure S7 shows the Sn $3d_{5/2}$, Ni 2p, Sn MNN spectra of the CNT-SnO$_2$(50)-NiO(200) (a, b, c) heterostructures and the Sn $3d_{5/2}$, Ni 2p, Ni LMM spectra of the CNT-NiO(200)-SnO$_2$(50) (d, e, f) heterostructures. In the case of CNT-SnO$_2$(50)-NiO(200), the Sn 3d intensity is strongly reduced as compared to that of SnO$_2$-terminated heterostructures (see survey XPS in **Figure S4**) but the peak shape and energy remains virtually identical to those of uncovered SnO$_2$, which demonstrates that NiO effectively covers the SnO$_2$ film. In addition, the Ni 2p and LMM spectra are also virtually identical to those measured when NiO is grown directly on CNTs, which suggests that the substrate does not strongly influence the formation of the NiO film away from the interface. For CNT-NiO(200)-SnO$_2$(50), we observe no more XPS signal from NiO, unambiguously demonstrating the homogenous coverage of the NiO film below SnO$_2$. There as well, the Sn 3d and MNN spectra are virtually identical both in terms of lineshape and peak position to those of SnO$_2$ grown directly onto the CNTs.
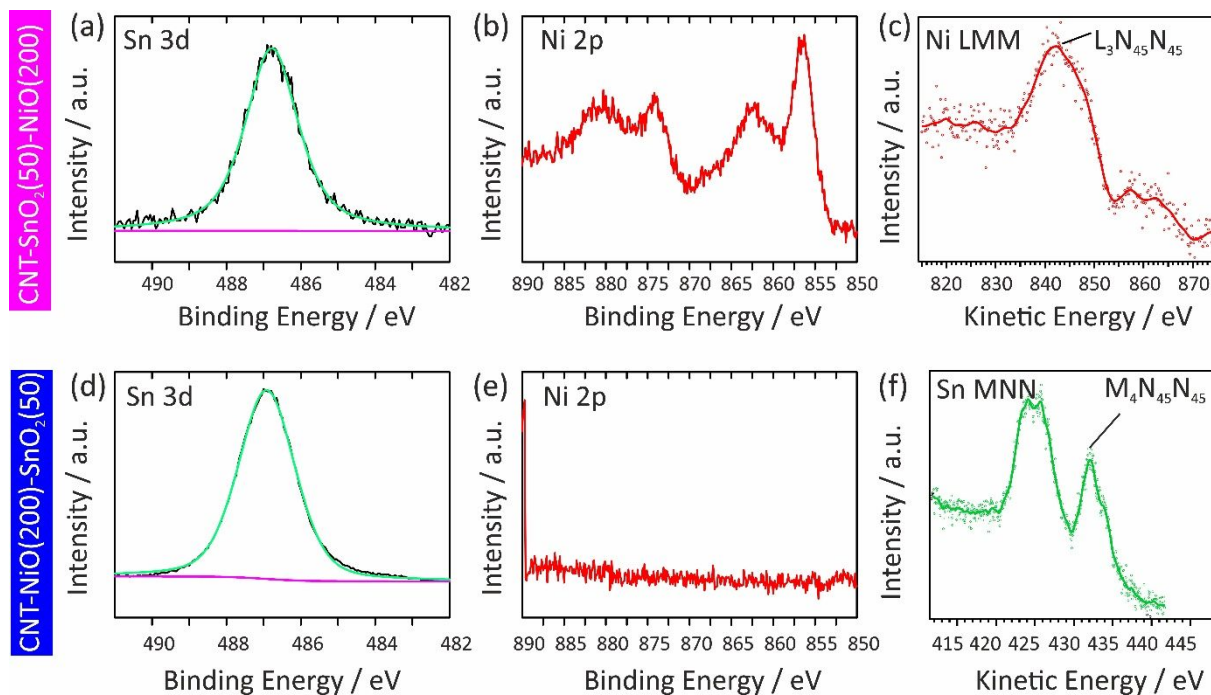
Figure S7. (a) Sn 3d, (b) Ni 2p and (c) Ni LMM spectra of CNT-SnO$_2$(50)-NiO(200) heterostructures. (d) Sn 3d (e) Ni 2p and (f) Sn MNN spectra of CNT-NiO(200)-SnO$_2$(50) heterostructures.

In order to ascertain the oxidation state of the metal in the as-grown metal oxides, we determined the modified Auger parameter α', with $\alpha' = E_b(2p_{3/2}) + E_k(L_3M_{45}M_{45})$ for Ni and $\alpha' = E_b(3d_{5/2}) + E_k(M_4N_{45}N_{45})$ for Sn. E_b represents the binding energy of the photoelectrons emitted from the Ni $2p_{3/2}$ or Sn $3d_{5/2}$ core levels and $E_k(L_3M_{45}M_{45})$ and $E_k(L_4M_{45}M_{45})$ is the kinetic energy of the corresponding Ni and Sn Auger electrons, respectively.[15-17] As compared to simply relying at the binding energy of a core level, the modified Auger parameter is a quantity that has the advantage of being independent of an absolute energy reference and has developed as an established method for determining the oxidation state of a given element.[16-17] To do so, the Auger electron E_k of the element under investigation is plotted against the core level E_b in a so-called Wagner plot, in which α' and the overall (E_B, E_k) position in the Wagner plot is representative of the formed compound and the related oxidation state of the element being investigated.[15,17] The obtained Wagner plots representative of the grown nickel and tin oxides in this work are plotted in **Figure S8a,b** together with those already published for other plausible Ni and Sn oxide compounds.[13,18] From this, it appears clearly that the surface of the as-grown and sputtered nickel oxide compounds consists of hydroxylated-NiO, Ni(OH)$_2$, and NiO, respectively, while the ALD of tin oxide results in the formation of SnO$_2$.
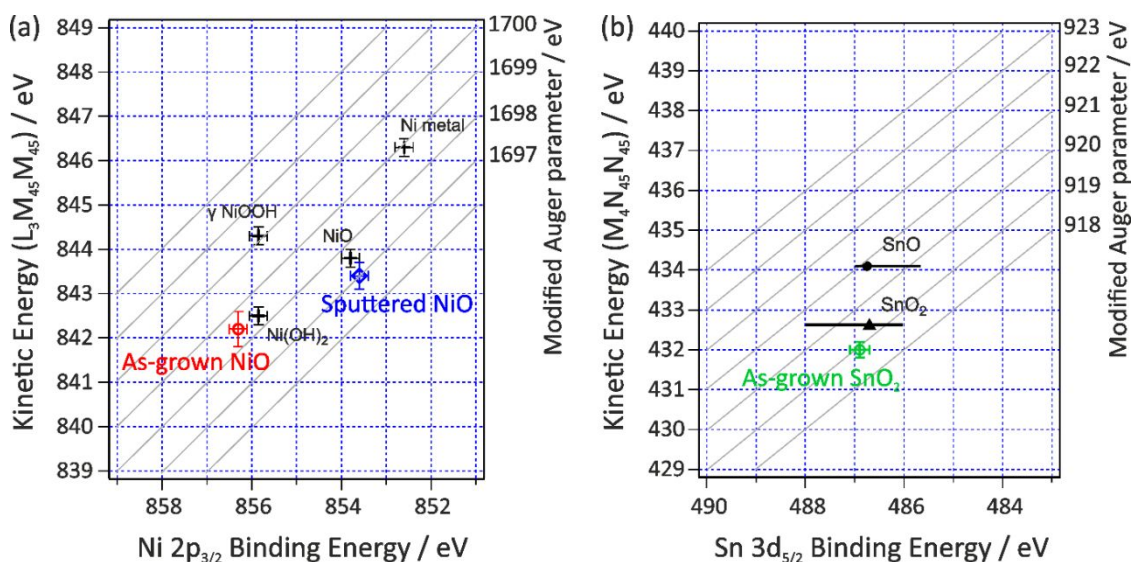
Figure S8. (a) Ni 2p$_{3/2}$–Ni L$_3$M$_{45}$M$_{45}$, and (b) Sn 3d$_{5/2}$–Sn M$_4$N$_{45}$N$_{45}$ Wagner (chemical state) plots including a comparison of the present data and literature (black symbols) adapted from the cited references.[13,18] Constant Auger parameter lines are also plotted together with their corresponding α′ values on the right side of the graph (grey-lines).

Having assessed that the formation of SnO$_2$ and hydroxide-terminated NiO films as a result of the ALD process, we now look at the XPS valence band features in. For SnO$_2$ grown on CNTs and NiO, we find that the valence band spectra present similar line-shape with the valence band onset at 2.45 eV ± 0.15 eV BE in good agreement with earlier studies.[10,19-20] In addition, we may observe an additional density of states peaking at ca. 2.15 eV BE and extending up to 1.55 eV BE, which could be attributed to surface states due to missing O atoms, **Figure S9a**. For hydroxylated NiO film grown on $_{50}$SnO$_2$/CNTs and CNTs, we again find very comparable spectra, also in good agreement with Ni(OH)$_2$/NiO spectra in the literature.[14] The valence band onsets of NiO are determined at 1.2 eV BE and 1.0 eV BE on CNT-SnO$_2$(50) and on CNTs, respectively, which is in the expected energy range for NiO, **Figure S9a**.[14,21] In addition, one notices a tail of states extended almost up to close the Fermi level (E$_F$), which might be due to the presence of NiO underneath the hydroxylated layer.[21] More surface sensitive ultraviolet photoelectron spectroscopy (UPS) measurements were then performed on as-grown and mildly sputtered CNT-NiO(200) . The results presented in **Figure S9b** on semi-log scale confirm that the valence band onsets are located at ca 1.1 eV BE and ca 0.2 eV BE for the as-grown and mildly sputtered CNT-NiO(200), respectively.
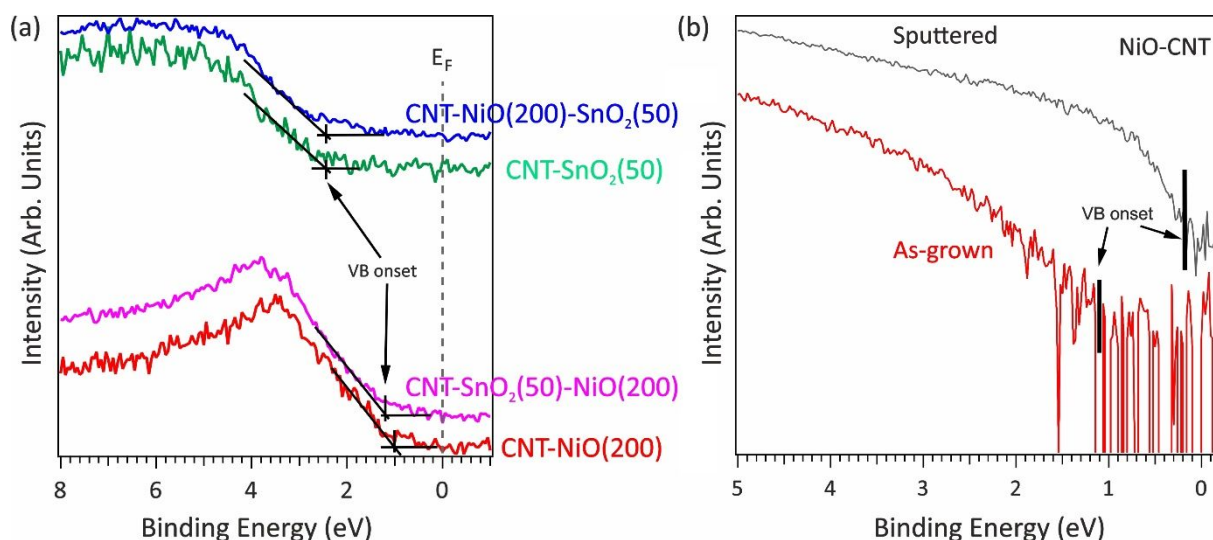
Figure S9. (a) XPS valence band spectra of CNT-NiO(200), CNT-SnO₂(50)-NiO(200), CNT-SnO₂(50) and CNT-NiO(200)-SnO₂(50). (b) UPS valence band spectra of CNT-NiO(200) before and after mild sputtering.

From these results, we found that the ALD growth sequence did not markedly impact the energy levels of the materials 'surface so that both sequence of deposition can be summarized in one diagram. Assuming bandgaps of 3.6 eV for SnO₂[22] and 3.6-4.2 eV for NiO,[23-25] we can draw in **Figure S10** the energy level diagram of the SnO₂/NiO and NiO/SnO₂ heterojunctions, which corresponds to that of a *p*-*n* junction in which SnO₂ and NiO are the *n*- and *p*-type semiconductors, respectively.
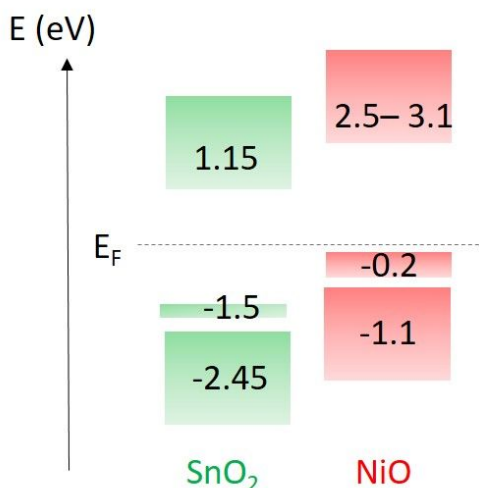

Figure S10. Energy level diagram of the SnO₂/NiO (or NiO/SnO₂) core-shell heterostructures including the experimentally determined valence energy levels of NiO (-0.2 eV), hydroxylated-NiO (-1.1 eV), SnO₂ (-2.45 eV) and SnOx-related surface states (-1.5 eV) and conduction energy level from literature.[22-25]

Gas Sensing Mechanism

The isothermal dynamic responses of all of the sensors fabricated with CNT-NiO(200), CNT-SnO₂(50), CNT-SnO₂(25)-NiO(200), CNT-SnO₂(50)-NiO(200), CNT-SnO₂(50)-NiO(350) and CNT-NiO(200)-SnO₂(50) were measured toward hydrogen (prototype of reducing gas) at

a temperature range 50 200 °C (**Figure S11,12**). The CNT-NiO(200) and CNT-SnO$_2$(50) sensors showed a typical *p*- (an increased in resistance induced by a reducing gas) and *n*-type (a decrease in resistance induced by a reducing gas) sensing response, respectively.[6,26-29]

The generally accepted gas sensing mechanism for MOS-based gas sensors is correlated with a change of electrical resistance/conductance of the system as a result of oxygen-mediated (chemisorbed oxygen species: O^{2-}, O$_2^-$ and O$^-$) interaction of gaseous analytes to the surface of the sensing films.[27,30-31] In the case of *n*-type MOS, the oxygen species absorbed onto the surface (by capturing electrons from the conduction band of *n*-type MOS) lead to the formation of an electron-depletion-layer (EDL) which induces an upward band bending and an increase in the electrical resistance of the system.[28,31-33] In the presence of a reducing gas such as hydrogen, the chemisorbed oxygen ions react with hydrogen species donating electrons back to the conduction band of *n*-type MOS (SnO$_2$).[25] This decreases the width of EDL and accordingly decreases the resistance of the system.[28,31,34]

In the case of a *p*-type MOS such as NiO, oxygen species withdraw electrons from the valence band of NiO, creating a hole-accumulation-layer (HAL), leading to a decrease of the resistance of the system.[6,31] In the presence of a reducing gas, such as hydrogen, reacts with chemisorbed oxygen ions, donating electrons back to the *p*-type MOS narrowing the HAL and thus increases the resistance of the system.[6,25,29,35]

In both of the CNT-NiO and CNT-SnO$_2$ CSHS in the current study, there is no direct contact between the CNTs-cores. *i.e.* CNT-CNT homojunction do not exist due to the confomal coatings achieved by ALD. Each CNT-MOS element is connected with another CNT-MOS element (*cf.* gas-sensing device fabrication and measurements section in the manuscript) by MOS shell-shell homojunctions (**Figure 3**).[6,33]

It is well known that composite materials, consisting of different metal oxides show different electrical properties and sensing behavior from their any of the single components. In the case of CNT-SnO$_2$-NiO or CNT-NiO-SnO$_2$ heterostructures, the interaction with the analytes occurs at the surface (whether NiO-terminated or SnO$_2$-terminated), *i.e.* the receptor function. On the other hand, the charge transport is affected (*i.e.* the transduction mechanism) due to the change of the contacts and accordingly the serial resistances. As a result, the deposition of NiO onto SnO$_2$ or *vice versa*, leads to the recombination of opposite charges at the *p-n* interface and thus an additional charge transport barriers is created, *i.e.* a Schottky barrier across the *n*(core)−*p*(shell) or *p*(shell) *n*(core) interface. The formation of a *p-n* heterojunction is traduced by the addition of a resistance element to the system, thus, it is expected that the resistance of the whole system increases.[6,25,35] Even though, in all CNT-MOS or CNT-MOS-MOS systems, the electrons flow through the CNT conductive core, the sensing-response is governed by the modulation of resistances of both MOS and of the one at the MOS-MOS interface (*cf.* **Figure 3**).[35-37] Due to the low resistance of the CNTs, the modulation of their resistance if any will not be significant and therefore would not affect the sensing-response.[6] The width of the depletion region (*L*) can be expressed as **equation (1)**.

$$L = \lambda_D \sqrt{\frac{2eV_c}{kT}} \qquad (1)$$

where λ_D is the Debye length of the material, eV_c is the surface potential, and kT is the thermal energy.[31,38] It demonstrates that L depends on the absorbed oxygen species and the electron density in the conduction band. Because the length of the depletion region is related directly to the λ_D, it demonstrates that the film will be fully depleted at a thickness comparable to the λ_D of the material.[6,25,35] Therefore, a film with a thickness comparable to the λ_D shows a pronounced modulation of the electrical conductance/resistance of the system and the surface depletion contribution becomes dominant. On the other hand, at higher shell thicknesses, the depletion of charge carriers is limited to the surface of the material and the contribution from the bulk of the material becomes important. Thus, it is well accepted that the sensing response can be optimized by optimizing the thickness (comparable to the Debye length of the material) of the films, where the film (shell-layer) fully participates in resistance/conductance modulation. The Debye length can be represented as **equation (2)**.[39-40]

$$\lambda_D = \sqrt{\frac{kT\varepsilon}{q^2 n_c}} \qquad (2)$$

Where k is the Boltzmann constant, ε is a dielectric constant, T is the absolute temperature, n_c is the carrier concentration and q is the electric charge [39]. Since λ_D depends also on the working temperature and on the concentration of charge carriers, the reported λ_D values for NiO and SnO$_2$ lay in a considerably large-range of 2 13[6,25,41-42] and 4 43 nm,[31,34,40,43] respectively.
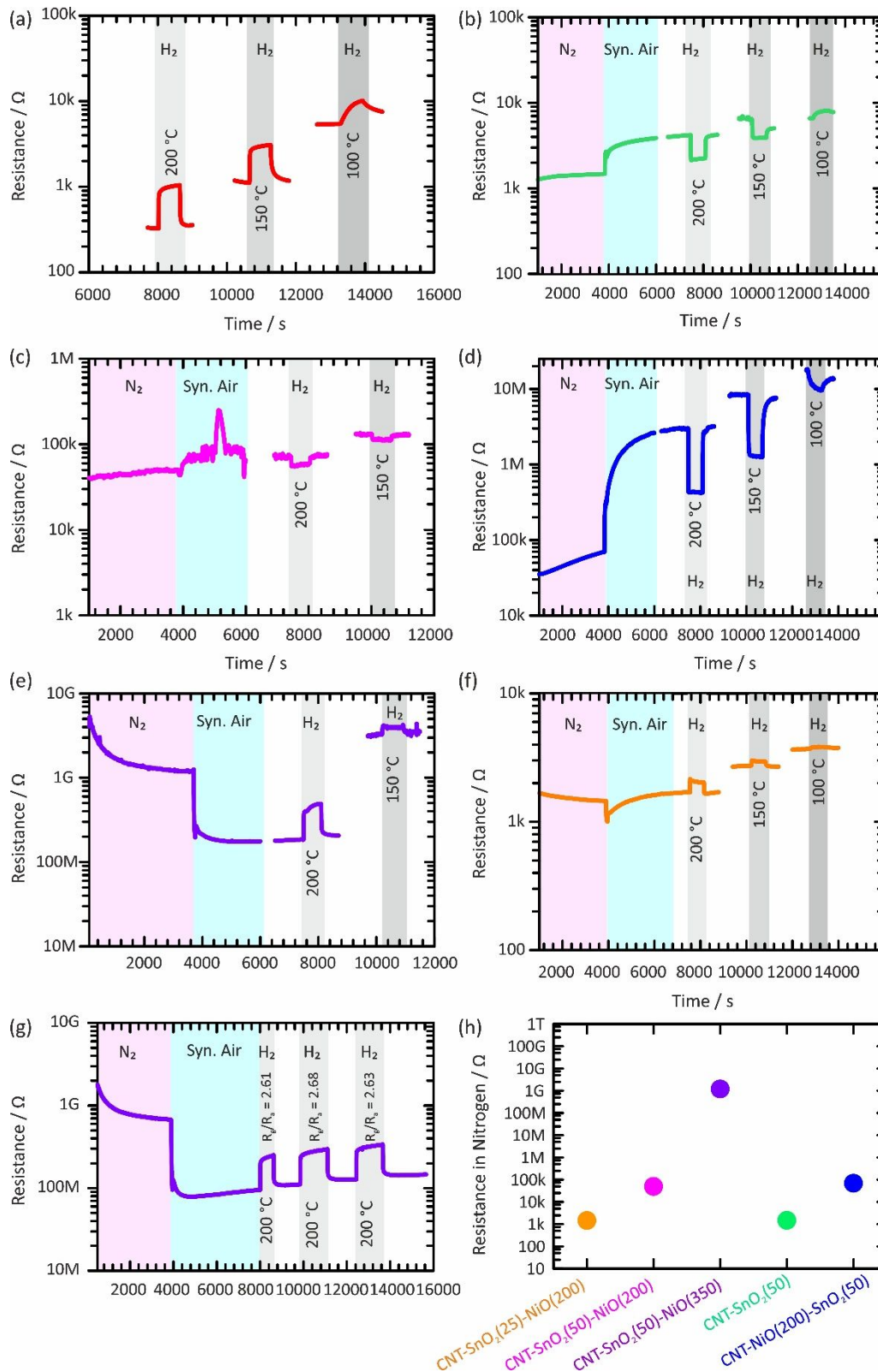
Figure S11. Transient response curves of all of the sensors fabricated at temperature ranges 100 – 200 °C toward H_2 (5000 ppm) in dry air, (a) CNT-NiO(200), (b) CNT-SnO_2(50), (c) CNT-SnO_2(50)-NiO(200), (d) CNT-NiO(200)-SnO_2(50), (e) CNT-SnO_2(50)-NiO(350) and (f) CNT-SnO_2(25)-NiO(200) core-shell heterostructures. (g) Transients for CNT-SnO_2(50)-NiO(350) sensor repeated at 200 °C, showing a good repeatability of the signals. (h) The baseline resistance of the sensors in nitrogen at 200 °C.
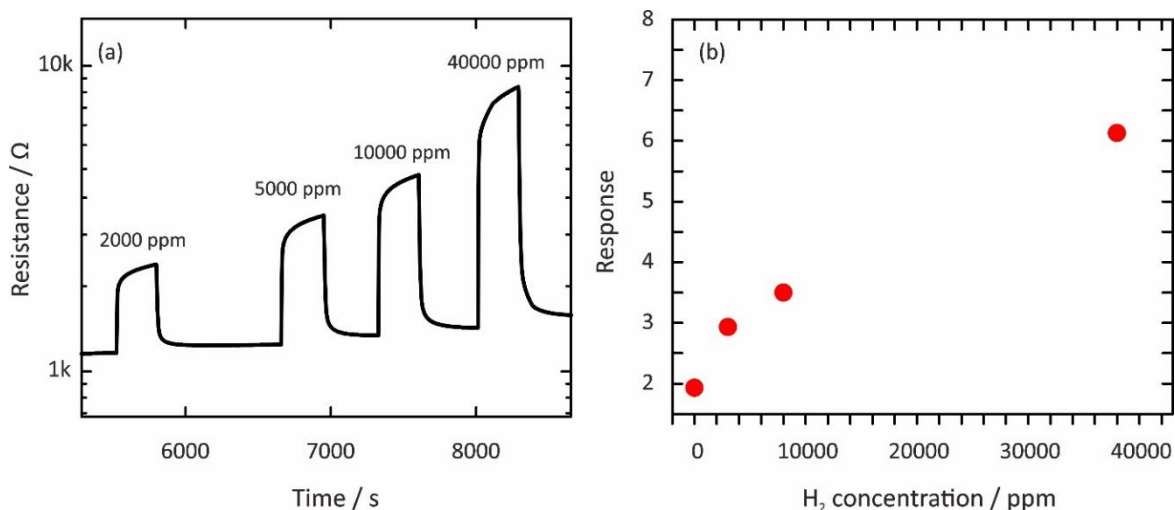
Figure S12. (a) Isothermal transient response curves for CNT-NiO(200) CSHS sensor at 200 °C toward different concentrations of H_2 (2000 40000 ppm) in dry air. (b) Responses as a function of hydrogen concentrations for CNT-NiO(200) sensor at 200 °C.

References

1.   Wu, Y.; Raza, M. H.; Chen, Y.-C.; Amsalem, P.; Wahl, S.; Skrodczky, K.; Xu, X.; Lokare, K. S.; Zhukush, M.; Gaval, P.; Koch, N.; Quadrelli, E. A.; Pinna, N., A Self-Limited Atomic Layer Deposition of WS2 Based on the Chemisorption and Reduction of Bis(t-butylimino)bis(dimethylamino) Complexes. *Chem. Mater.* **2019,** *31* (6), 1881-1890.

2.   Fan, Y.; Wu, Y.; Clavel, G.; Raza, M. H.; Amsalem, P.; Koch, N.; Pinna, N., Optimization of the Activity of Ni-Based Nanostructures for the Oxygen Evolution Reaction. *ACS Appl. Energy Mater.* **2018,** *1* (9), 4554-4563.

3.   Marichy, C.; Tessonnier, J.-P.; Ferro, M. C.; Lee, K.-H.; Schlögl, R.; Pinna, N.; Willinger, M.-G., Labeling and Monitoring the Distribution of Anchoring Sites on Functionalized CNTs by Atomic Layer Deposition. *J. Mater. Chem.* **2012,** *22* (15), 7323-7330.

4.   Marichy, C.; Pucci, A.; Willinger, M. G.; Pinna, N. Coating of Carbon Nanotubes. In Atomic Layer Deposition of Nanostructured Materials; Pinna, N., Knez, M., Eds.; Wiley-VCH Verlag GmbH & Co. KGaA: Weinheim, Germany, 2012; pp 327−343.

5.   Marichy, C.; Pinna, N., Carbon-nanostructures Coated/Decorated by Atomic Layer Deposition: Growth and Applications. *Coord. Chem. Rev.* **2013,** *257* (23), 3232-3253.

6.   Raza, M. H.; Movlaee, K.; Leonardi, S. G.; Barsan, N.; Neri, G.; Pinna, N., Gas Sensing of NiO-SCCNT Core–Shell Heterostructures: Optimization by Radial Modulation of the Hole-Accumulation Layer. *Adv. Funct. Mater.* **2020,** *30* (6), 1906874.

7.   Pinna, N., X-Ray Diffraction from Nanocrystals. In *Scattering Methods and the Properties of Polymer Materials*, Stribeck, N.; Smarsly, B., Eds. Springer Berlin Heidelberg: Berlin, Heidelberg, **2005**, pp 29-32.

8.   Raza, M. H.; Movlaee, K.; Wu, Y.; El-Refaei, S. M.; Karg, M.; Leonardi, S. G.; Neri, G.; Pinna, N., Tuning the NiO Thin Film Morphology on Carbon Nanotubes by Atomic Layer Deposition for Enzyme-Free Glucose Sensing. *ChemElectroChem* **2019,** *6* (2), 383-392.

9.   Kövér, L.; Kovács, Z.; Sanjinés, R.; Moretti, G.; Cserny, I.; Margaritondo, G.; Pálinkás, J.; Adachi, H., Electronic Structure of Tin Oxides: High-resolution Study of XPS and Auger Spectra. *Surf. Interface Anal.* **1995,** *23* (7-8), 461-466.

10.   Themlin, J.-M.; Chtaïb, M.; Henrard, L.; Lambin, P.; Darville, J.; Gilles, J.-M., Characterization of Tin Oxides by X-ray-Photoemission Spectroscopy. *Phys. Rev. B* **1992,** *46* (4), 2460-2466.

11.   Stranick, M. A.; Moskwa, A., SnO2 by XPS. *Surf. Sci. Spectra* **1993,** *2* (1), 50-54.

12.   Alders, D.; Voogt, F. C.; Hibma, T.; Sawatzky, G. A., Nonlocal Screening Effects in 2p X-ray Photoemission Spectroscopy of NiO (100). *Phys. Rev. B* **1996,** *54* (11), 7716-7719.

13.   Biesinger, M. C.; Lau, L. W. M.; Gerson, A. R.; Smart, R. S. C., The Role of the Auger Parameter in XPS Studies of Nickel Metal, Halides and Oxides. *PCCP* **2012,** *14* (7), 2434-2442.

14.   Greiner, M. T.; Helander, M. G.; Wang, Z.-B.; Tang, W.-M.; Lu, Z.-H., Effects of Processing Conditions on the Work Function and Energy-Level Alignment of NiO Thin Films. *J. Phys. Chem. C* **2010,** *114* (46), 19777-19781.

15.   Wagner, C. D., Auger Lines in X-ray Photoelectron Spectrometry. *Anal. Chem.* **1972,** *44* (6), 967-973.

16.   Gaarenstroom, S. W.; Winograd, N., Initial and Final State Effects in the ESCA Spectra of Cadmium and Silver Oxides. *The Journal of Chemical Physics* **1977,** *67* (8), 3500-3506.

17.   Wagner, C. D.; Gale, L. H.; Raymond, R. H., Two-dimensional Chemical State Plots: a Standardized Data Set for Use in Identifying Chemical States by X-ray Photoelectron Spectroscopy. *Anal. Chem.* **1979,** *51* (4), 466-482.

18.   NIST X-ray Photoelectron Spectroscopy Database, NIST Standard Reference Database Number 20, National Institute of Standards and Technology, Gaithersburg MD, 20899. **2000**.

19.   Grządziel, L.; Krzywiecki, M.; Szwajca, A.; Sarfraz, A.; Genchev, G.; Erbe, A., Detection of Intra-Band Gap Defects States in Spin-Coated Sol-Gel SnOx Nanolayers by Photoelectron Spectroscopies. *J. Phys. D: Appl. Phys.* **2018,** *51* (31), 315301.

20.   Cox, D. F.; Fryberger, T. B.; Semancik, S., Oxygen vacancies and defect electronic states on the SnO2 (110)-1×1 surface . *Phys. Rev. B* **1988,** *38* (3), 2072-2083.

21.   Fingerle, M.; Tengeler, S.; Calvet, W.; Jaegermann, W.; Mayer, T., Sputtered Nickel Oxide Thin Films on n-Si(100)/SiO2 Surfaces for Photo-Electrochemical Oxygen Evolution Reaction (OER): Impact of Deposition Temperature on OER Performance and on Composition before and after OER. *J. Electrochem. Soc.* **2020,** *167* (13), 136514.

22.   Ganose, A. M.; Scanlon, D. O., Band Gap and Work Function Tailoring of SnO2 for Improved Transparent Conducting Ability in Photovoltaics. *Journal of Materials Chemistry C* **2016,** *4* (7), 1467-1475.

23.   Sagadevan, S.; Rajesh, S.; Das, I., Studies on Nanocrystalline Nickel Oxide Thin Films for Potential Applications. *Materials Today: Proceedings* **2017,** *4* (2, Part A), 4123-4129.

24.   Hüfner, S., Electronic Structure of NiO and Related 3d-Transition-Metal Compounds. *Adv. Phys.* **1994,** *43* (2), 183-356.

25.   Raza, M. H.; Kaur, N.; Comini, E.; Pinna, N., Toward Optimized Radial Modulation of the Space-Charge Region in One-Dimensional SnO2–NiO Core–Shell Nanowires for Hydrogen Sensing. *ACS Appl. Mater. Interfaces* **2020,** *12* (4), 4594-4606.

26.   Elger, A.-K.; Hess, C., Elucidating the Mechanism of Working SnO2 Gas Sensors Using Combined Operando UV/Vis, Raman, and IR Spectroscopy. *Angew. Chem. Int. Ed.* **2019,** *58* (42), 15057-15061.

27.   Degler, D.; Wicker, S.; Weimar, U.; Barsan, N., Identifying the Active Oxygen Species in SnO2 Based Gas Sensing Materials: An Operando IR Spectrsocopy Study. *J. Phys. Chem. C* **2015,** *119* (21), 11792-11799.

28.   Staerz, A.; Suzuki, T.; Weimar, U.; Barsan, N., 12 - SnO2: The Most Important Base Material for Semiconducting Metal Oxide-Based Materials. In *Tin Oxide Materials*, Orlandi, M. O., Ed. Elsevier: **2020**, pp 345-377.

29.   Budde, M.; Tschammer, C.; Franz, P.; Feldl, J.; Ramsteiner, M.; Goldhahn, R.; Feneberg, M.; Barsan, N.; Oprea, A.; Bierwagen, O., Structural, Optical, and Electrical Properties of Unintentionally Doped NiO Layers Grown on MgO by Plasma-assisted Molecular Beam Epitaxy. *J. Appl. Phys.* **2018,** *123* (19), 195301.

30.   Zhang, J.; Zeng, D.; Zhu, Q.; Wu, J.; Huang, Q.; Zhang, W.; Xie, C., Enhanced Room Temperature NO2 Response of NiO–SnO2 Nanocomposites Induced by Interface Bonds at the p–n Heterojunction. *PCCP* **2016,** *18* (7), 5386-5396.

31.   Barsan, N.; Weimar, U., Conduction Model of Metal Oxide Gas Sensors. *J. Electroceram.* **2001,** *7* (3), 143-167.

32.   Russo, P. A.; Donato, N.; Leonardi, S. G.; Baek, S.; Conte, D. E.; Neri, G.; Pinna, N., Room-Temperature Hydrogen Sensing with Heteronanostructures Based on Reduced Graphene Oxide and Tin Oxide. *Angew. Chem. Int. Ed.* **2012,** *51* (44), 11053-11057.

33.   Marichy, C.; Russo, P. A.; Latino, M.; Tessonnier, J.-P.; Willinger, M.-G.; Donato, N.; Neri, G.; Pinna, N., Tin Dioxide–Carbon Heterostructures Applied to Gas Sensing: Structure-Dependent Properties and General Sensing Mechanism. *J. Phys. Chem. C* **2013,** *117* (38), 19729-19739.

34.   Ogawa, H.; Nishikawa, M.; Abe, A., Hall Measurement Studies and an Electrical Conduction Model of Tin Oxide Ultrafine Particle Films. *J. Appl. Phys.* **1982,** *53* (6), 4448-4455.

35.   Degler, D.; Weimar, U.; Barsan, N., Current Understanding of the Fundamental Mechanisms of Doped and Loaded Semiconducting Metal-Oxide-Based Gas Sensing Materials. *ACS Sens.* **2019,** *4* (9), 2228-2249.

36.   Staerz, A.; Gao, X.; Cetmi, F.; Ming, Z.; Weimar, U.; Zhang, T.; Barsan, N., Dominant Role of Heterojunctions in Gas Sensing with Composite Materials. *ACS Appl. Mater. Interfaces* **2020,** *12* (18), 21127-21132.

37.   Karnati, P.; Akbar, S.; Morris, P. A., Conduction Mechanisms in One Dimensional Core-Shell Nanostructures for Gas Sensing: A Review. *Sens. Actuators, B* **2019,** *295*, 127-143.

38.   Horrillo, M. C.; Gutiérrez, J.; Arés, L.; Robla, J. I.; Sayago, I.; Getino, J.; Agapito, J. A., Hall Effect Measurements to Calculate the Conduction Control in Semiconductor Films of SnO2. *Sensors and Actuators A: Physical* **1994,** *42* (1), 619-621.

39.   Zhu, L.-Y.; Yuan, K.; Yang, J.-G.; Ma, H.-P.; Wang, T.; Ji, X.-M.; Feng, J.-J.; Devi, A.; Lu, H.-L., Fabrication of Heterostructured p-CuO/n-SnO2 Core-Shell Nanowires for Enhanced Sensitive and Selective Formaldehyde Detection. *Sens. Actuators, B* **2019,** *290*, 233-241.

40.   Mills, S.; Lim, M.; Lee, B.; Misra, V., Atomic Layer Deposition of SnO2for Selective Room Temperature Low ppb Level O3Sensing. *ECS Journal of Solid State Science and Technology* **2015,** *4* (10), S3059-S3061.

41.   Seo, S.; Park, I. J.; Kim, M.; Lee, S.; Bae, C.; Jung, H. S.; Park, N.-G.; Kim, J. Y.; Shin, H., An Ultra-Thin, Un-Doped NiO Hole Transporting Layer of Highly Efficient (16.4%) Organic-Inorganic Hybrid Perovskite Solar Cells. *Nanoscale* **2016,** *8* (22), 11403-11412.

42.   Xu, Q.; Zhang, Z.; Song, X.; Yuan, S.; Qiu, Z.; Xu, H.; Cao, B., Improving the Triethylamine Sensing Performance Based on Debye Length: A Case Study on α-Fe2O3@NiO(CuO) Core-Shell Nanorods Sensor Working at Near Room-Temperature. *Sens. Actuators, B* **2017,** *245*, 375-385.

43.   Ng, S.; Prášek, J.; Zazpe, R.; Pytlíček, Z.; Spotz, Z.; Pereira, J. R.; Michalička, J.; Přikryl, J.; Krbal, M.; Sopha, H.; Hubálek, J.; Macák, J. M., Atomic Layer Deposition of SnO2-Coated Anodic One-Dimensional TiO2 Nanotube Layers for Low Concentration NO2 Sensing. *ACS Appl. Mater. Interfaces* **2020,** *12* (29), 33386-33396.